Supplementary Information (SI) for Nanoscale.

Supplementary Information

Determination of the rate equations for erbium nanoparticles at arbitrary concentrations and drastically enhanced non-radiative transitions

Jinhua Wu[a,b$], Zhang Liang[a,b,$], Hao Sun[b], Ying Cui[b], and Cun-Zheng Ning[a,b*]

[a] *College of Integrated Circuits and Optoelectronic Chips, Shenzhen Tech. University, Shenzhen, 518118, China*

[b] *Department of Electronic Engineering, Tsinghua University, Beijing, 100084, China*

**Correspondence to: ningcunzheng@sztu.edu.cn*

[$] *equal contribution authors*

I. Material characterization of the core and core-shell nanoparticles. 2

II. QY measurement. 5

III. Spectrum quantification of upconversion (UC) and down-conversion (DC) emissions. 7

IV. Time-resolved emission measurement. 9

V. Rate equation simulation of NaEr$_x$Y$_{1-x}$F$_4$@NaYF$_4$ nanoparticles. 10

VI. Power-dependent simulated characteristics of decay curves. 14

VII. Emission enhancement of core-shell structure. 15

VIII. Rate equation simulation of ENPCs. 17

IX. Results of simulated parameters. 22

X. Analytical calculation of simplified rate equations. 25

References 27

I. Material characterization of the core and core-shell nanoparticles.

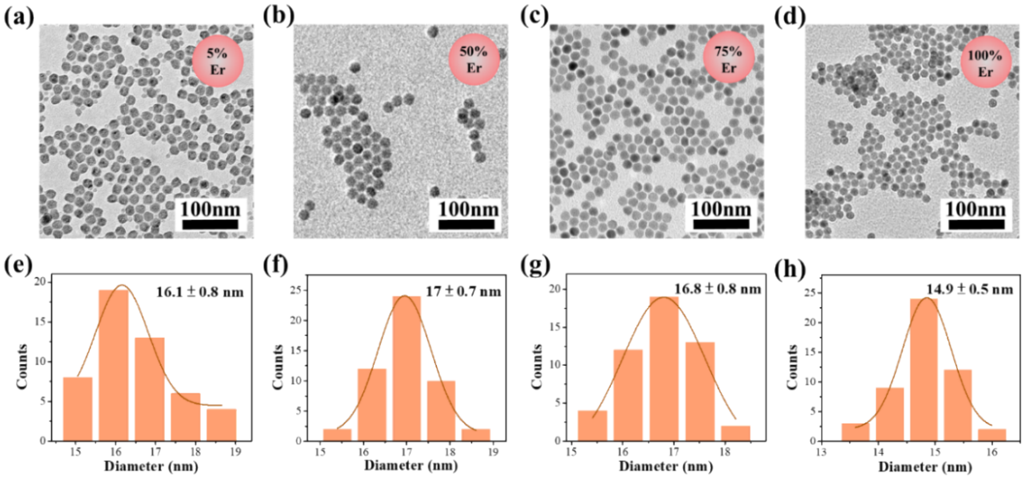

Figure S1. Transmission electron microscopy (TEM) images and corresponding size distributions of $NaEr_xY_{1\text{-}x}F_4$ (x=5, 50, 75, 100 %) nanoparticles. (a & e) $NaEr_{0.05}Y_{0.95}F_4$, (b & f) $NaEr_{0.5}Y_{0.5}F_4$, (c & g) $NaEr_{0.75}Y_{0.25}F_4$, (d & h) $NaErF_4$.

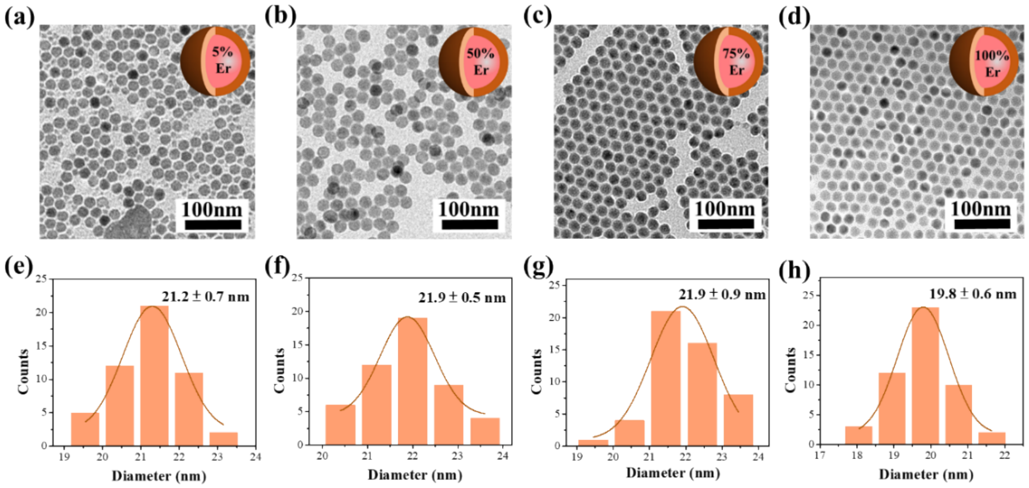

Figure S2. TEM images and corresponding size distributions of $NaEr_xY_{1\text{-}x}F_4$@NaYF4 (x=5, 50, 75, 100 %) core-shell nanoparticles. (a & e) $NaEr_{0.05}Y_{0.95}F_4$@$NaYF_4$, (b & f) $NaEr_{0.5}Y_{0.5}F_4$@$NaYF_4$, (c & g) $NaEr_{0.75}Y_{0.25}F_4$@$NaYF_4$, (d & h) $NaErF_4$@$NaYF_4$.

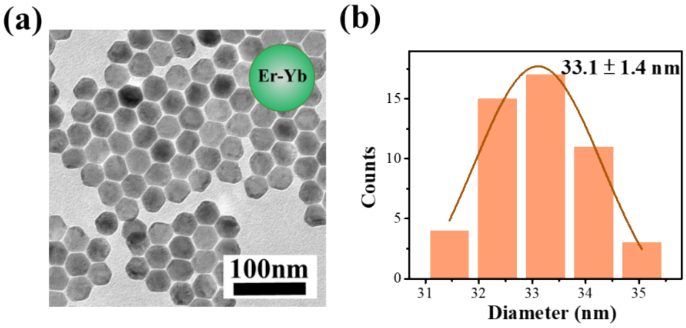

Figure S3. TEM images and corresponding size distributions of $NaEr_{0.02}Yb_{0.2}Y_{0.78}F_4$ composition.

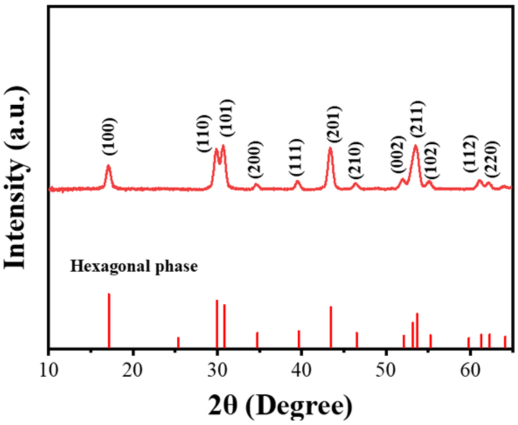

Figure S4. Representative powder X-ray Diffraction (XRD) pattern of the $NaEr_{0.75}Y_{0.25}F_4$ nanoparticles confirming the hexagonal phase, indexed to JCPDS file #28-1192.

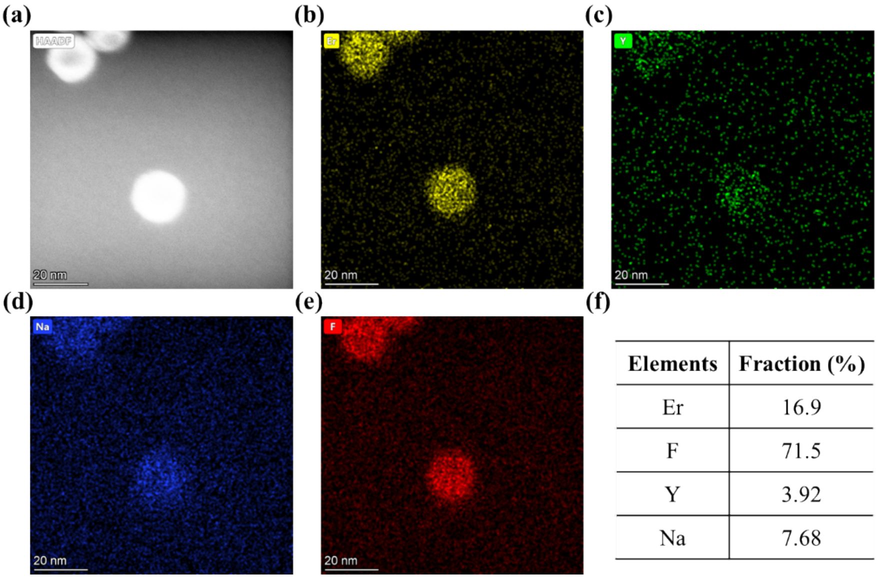

Elements	Fraction (%)
Er	16.9
F	71.5
Y	3.92
Na	7.68

Figure S5. (a) HAADF-STEM image of the $NaEr_{0.75}Y_{0.25}F_4$ nanoparticles. (b–e) EDS maps corresponding to (e). (f) Atom fraction of different elements.

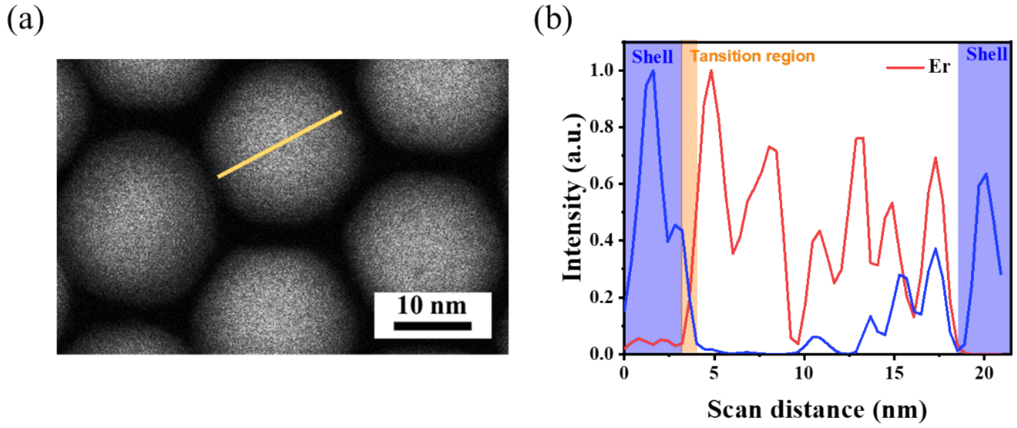

Figure S6. (a) STEM image of the core-shell nanocrystals. The yellow line indicates the direction of the EDS line scanning. (b) EDS spectra of Er elements.

To determine the distribution of Er elements in the core-shell structure, we measured the EDS spectra for erbium across the structure and presented in **Fig. S6**, where we find that the erbium element is highly concentrated in the core layer with a transition region into the shell less than 1 nm. As the data in our EDS equipment provides an averaged chemical composition based on the electron-beam detection, we recommend the more refined EDS analysis using the subshell approach in the reference[1].

II. QY measurement.

The typical measurements of QY are performed in the integrated sphere system following the reported method[2], including the integrated sphere, optical fiber, spectrometer, detector, and other optical components, as shown in **Fig. S7**.

The absolute QY Φ is defined as:

$$\Phi = \frac{E}{A} = \frac{\int_{\lambda_{em1}}^{\lambda_{em2}} \left(\frac{I_s(\lambda_{em}) - I_b(\lambda_{em})}{S(\lambda_{em})} \right) \lambda_{em} d\lambda_{em}}{\int_{\lambda_{ex1}}^{\lambda_{ex2}} \left(\frac{I_b(\lambda_{ex}) - I_s(\lambda_{ex})}{S(\lambda_{ex})} \right) \lambda_{ex} d\lambda_{ex}}$$

Where E and A are the emitted photons and absorbed photons, respectively. I_s and I_b are the spectra for the nanoparticles sample and blank sample, respectively. $S(\lambda)$ is the calibrated spectrum responsivity. λ_{em1}-λ_{em2} (λ_{ex1}-λ_{ex2}) denotes the spectra range of emission (excitation).

1) We first verified the linearity of the entire detection system and calibrated the responsivity using a NIST-traceable radiometric calibration source (Ocean Optics, HL-cal-3plus, Serial Number 7003P1261, Certificate Number 29884). Once we obtain the spectral signal $I(\lambda)$ and the calibrated spectral irradiance $L(\lambda)$ of the light source, the spectral responsivity can be defined as $S(\lambda)=I(\lambda)/L(\lambda)$.

2) Place a cuvette with a certain amount of cyclohexane as a blank control in the center of the integrated sphere and insert an edge filter in front of the entrance slit. The emission spectra $I_b(\lambda_{em})$ is then captured.

3) Replace the edge filter with a suitable neutral density filter to obtain the excitation spectra $I_b(\lambda_{ex})$.

4) Replace the blank sample with the cuvette containing the nanoparticles sample, and repeat the same procedure to obtain the emission spectra $I_s(\lambda_{em})$ and the excitation spectra $I_s(\lambda_{ex})$.

Each test was repeated five times and completed as quickly as possible to reduce the thermal effect of excitation.

The uncertainty of QY $\Delta\Phi$ is described by:

$$\Delta\Phi = \Phi\sqrt{\left(\frac{\Delta E}{E}\right)^2 + \left(\frac{\Delta A}{A}\right)^2}$$

Where the ΔE and ΔA are the uncertainties of E and A, which are defined as:

$$\Delta E = \frac{t_p}{\sqrt{n}}\sqrt{\frac{\sum_{i=1-5}(E_i - E)^2}{n-1}}$$

$$\Delta A = \frac{t_p}{\sqrt{n}}\sqrt{\frac{\sum_{i=1-5}(A_i - A)^2}{n-1}}$$

Where E_i and A_i are the values of each test, n is the number of tests (equal to 5 in this case), t_p is the test statistic for different amounts of data at the 95% confidence level, which is equal to 2.78[3].

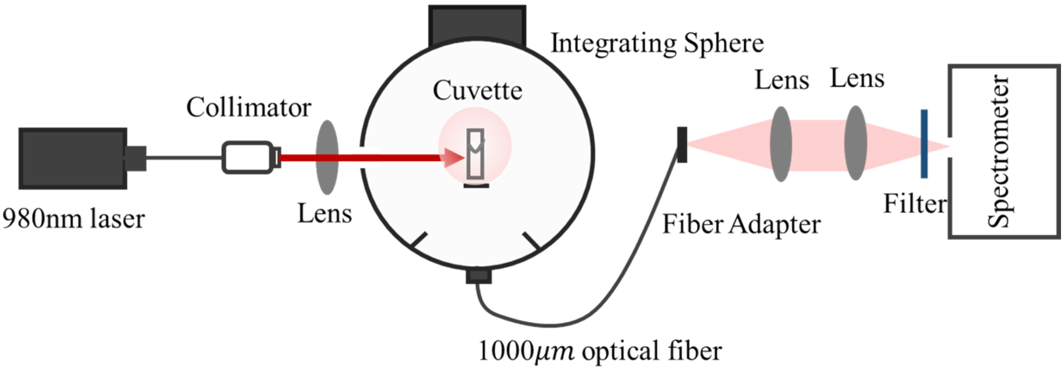

Figure S7. Schematic diagram of the integrated sphere system

III. Spectrum quantification of upconversion (UC) and down-conversion (DC) emissions.

Measurements of the quantitative emissions were performed in an optical microscope system, as shown in **Fig.S8**.

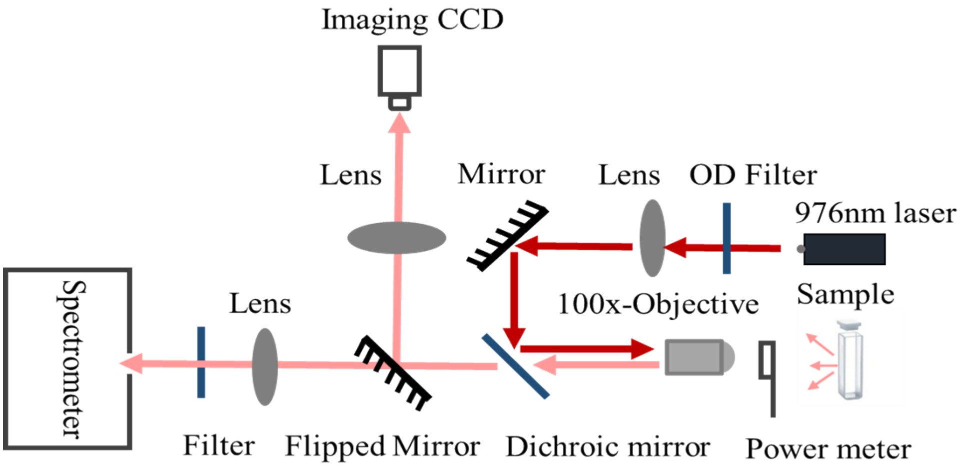

Figure S8. Schematic illustration of the microscope system.

For the typical UC emission measurements, a 980 nm collimated excitation laser was used as the pumping source, the power of which was controlled by a continuously variable neutral density filter (Thorlabs, NDC-100C-4M). The excitation light was reflected by a short-pass dichroic mirror (Thorlabs, DMSP950) and focused by a 50x objective with NA=0.7. The emission from the sample was collected by the same objective and passed through the dichroic mirror. A flip mirror was inserted into the collection beam path to either reflect the emitted light to a CCD camera or a spectrometer. A short-pass filter (Thorlabs, FESH0900) was used in front of the spectrometer to cut off the excitation laser. A spectrometer (Princeton, Acton SP2750) equipped with a Si CCD (Princeton, PYLoN) was used for UC measurement. For DC measurements, the spectrometer (Princeton, Acton SP2500) equipped with an InGaAs CCD (Princeton, PYLoN-IR) was used, along with a long-pass dichroic mirror (Thorlabs, DMLP1180) and a long-pass filter (Thorlabs, FEL1000).

To calibrate the collection efficiency of the microscope setup, we use multiple lasers at 532 nm, 633 nm, and 1525 nm, considering the different energy levels with the narrow bandwidth of Er. The optical system is the same as shown in **Fig.S8,** except that the sample is replaced by a diffuse reflector. The diffuser plate coated with highly reflective Spectralon material simulates the emission of the sample. First, a power meter at the focal plane is used to calibrate the power value of the laser irradiated on the plate, and the diffuser plate on the stage is adjusted to a suitable position at the focal plane in CCD imaging mode. The light is then collected by the objective, passes through a series of optical elements, and enters the slit of the spectrometer. The collection efficiency η of the entire system is defined as

$$\eta = \frac{\mathrm{C}_{\mathrm{int}}}{2 * pt / hv}$$

where C_{int} denotes the integral value of the spectral area, p is the power of excitation laser, t is the exposure time, h is the Planck constant, and v represents the frequency of the light.

We can unify UC and DC optical systems by calibrating the system efficiency at different wavelengths. Based on the spectral responsivity, we can calculate the absolute energies for UC and DC emissions in the integrating sphere system.

IV. Time-resolved emission measurement.

The schematic diagram of the time-resolved measurement setup is shown in **Fig.S9.** A CW laser at 980nm (MDL-XF-980-6W) was used as the excitation source and modulated at a frequency of 20 Hz using a digital pulse generator (DG535). For the measurement of UC and DC emission, a short pass filter (Thorlabs, FESH0900) or a long pass filter (Thorlabs, FEL1000) was selected and used as the edge-pass filter to cut off the 980 nm laser, respectively. A Si detector (OE-300-SI-10) was used to detect the UC emission bands at different energy levels selected by different bandpass filters (Thorlabs, FB550-40, FB650-40, FB800-40, FB850-40). An InGaAs detector (OE-300-IN-10) was used to detect the DC emission at 1.5 μm. The oscilloscope (Tektronix, Mso5204B) was synchronized with the trigger signal of the digital pulse generator to obtain the voltage output from each detector.

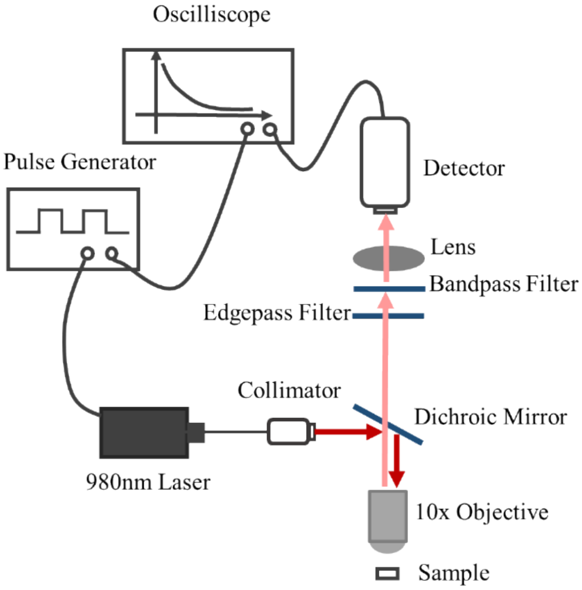

Figure S9. Schematic diagram of the time-resolved measurement setup.

V. Rate equation simulation of NaEr$_x$Y$_{1\text{-}x}$F$_4$@NaYF$_4$ nanoparticles.

Based on past investigations and the characteristics of high Er concentrations, we considered the most relevant ET processes with matching energy gaps in our model. We have listed all ET processes that match with 980 nm excitation. For energy matching at 1.5 μm, we included the intense $(\mathrm{I}_{15/2}, {}^4\mathrm{I}_{9/2})\leftrightarrow({}^4\mathrm{I}_{13/2}, {}^4\mathrm{I}_{13/2})$ processes, which are prevalent due to the abundant population at the 4I13/2 energy level. The $({}^4\mathrm{I}_{13/2}, {}^2\mathrm{H}_{11/2})\leftrightarrow({}^4\mathrm{I}_{9/2}, {}^4\mathrm{I}_{9/2})$ and $({}^4\mathrm{I}_{15/2}, {}^2\mathrm{H}_{11/2})\leftrightarrow({}^4\mathrm{I}_{13/2}, {}^4\mathrm{I}_{9/2})$ processes were ignored because they involve limited population. Additionally, the $({}^4\mathrm{I}_{9/2}, {}^4\mathrm{S}_{3/2})\leftrightarrow({}^4\mathrm{F}_{9/2}, {}^4\mathrm{F}_{9/2})$ process, with a matching energy gap, may play an important role in red emission at high Er concentrations^4. To objectively analyze population pathways in high-concentration systems, we intentionally included the $({}^4\mathrm{I}_{9/2}, {}^4\mathrm{S}_{3/2})\leftrightarrow({}^4\mathrm{F}_{9/2}, {}^4\mathrm{F}_{9/2})$ process in our model. According to the energy diagram in **Fig.2a**, the population N$_\mathrm{i}$ of certain Er energy level in ENPCNs is described as

$$\frac{dN_0}{dt} = W_{10}N_1 + \sum_{i=1}^{7} A_{i0}N_i + k_{13}N_1^2 + \left(k_{14}N_1 + k_{26}N_2 + k_{47}N_4 + k_{58}N_5\right)N_2$$
$$-\left(\sigma_{02}\rho + k_{31}N_3 + k_{62}N_6 + k_{84}N_8\right)N_0$$

$$\frac{dN_1}{dt} = W_{21}N_2 + \sum_{i=2}^{7} A_{i1}N_i + 2k_{31}N_3N_0 - \left(W_{10} + A_{10} + k_{14}N_2\right)N_1 - 2k_{13}N_1^2$$

$$\frac{dN_2}{dt} = \sigma_{02}\rho N_0 + W_{32}N_3 + \sum_{i=4}^{7} A_{i2}N_i + k_{84}N_8N_0 + 2k_{62}N_6N_0$$
$$-\left(W_{21} + \sigma_{26}\rho + \sum_{j=0}^{1} A_{2j} + k_{14}N_1 + 2k_{26}N_2 + k_{47}N_4 + k_{58}N_5\right)N_2$$

$$\frac{dN_3}{dt} = W_{43}N_4 + \sum_{i=5}^{7} A_{i3}N_i + k_{13}N_1^2 - \left(W_{32} + \sum_{j=0}^{1} A_{3j} + k_{31}N_0 + k_{54}N_5\right)N_3$$

$$\frac{dN_4}{dt} = W_{54}N_5 + A_{74}N_7 + k_{14}N_1N_2 + k_{84}N_0N_8 + 2k_{54}N_3N_5 - \left(W_{43} + \sum_{j=0}^{2} A_{4j} + k_{47}N_2\right)N_4$$

$$\frac{dN_5}{dt} = W_{65}N_6 - \left(W_{54} + \sum_{j=0}^{3} A_{5j} + k_{58}N_2 + k_{54}N_3 + \sigma_{58}\rho\right)N_5$$

$$\frac{dN_6}{dt} = \sigma_{26}\rho N_2 + W_{76}N_7 + k_{26}N_2^2 - \left(W_{65} + \sum_{j=0}^{3} A_{6j} + k_{62}N_0 \right) N_6$$

$$\frac{dN_7}{dt} = W_{87}N_8 + k_{47}N_2N_4 - \left(W_{76} + \sum_{j=0}^{4} A_{7j} \right) N_7$$

$$\frac{dN_8}{dt} = \sigma_{58}\rho N_5 + k_{58}N_2N_5 - \left(W_{87} + k_{84}N_0 \right) N_8$$

$$N_{Er} = N_0 + N_1 + N_2 + N_3 + N_4 + N_5 + N_6 + N_7 + N_8$$

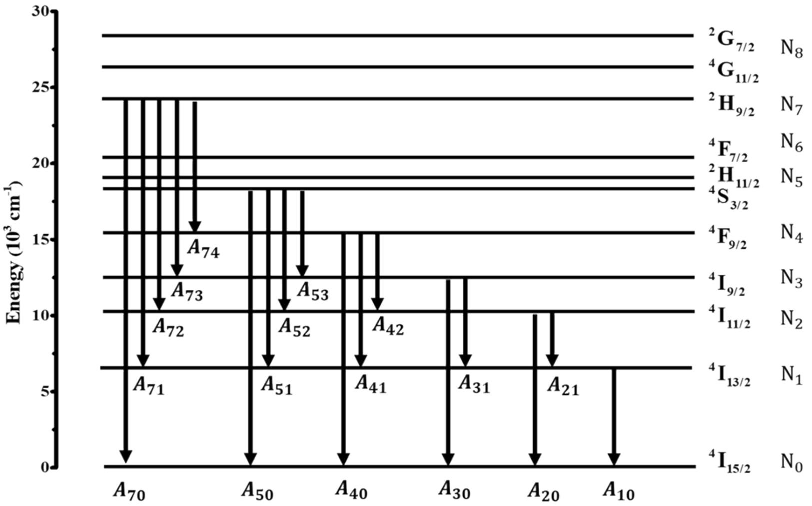

Figure S10. Schematic diagram of the spontaneous processes in the REs Model.

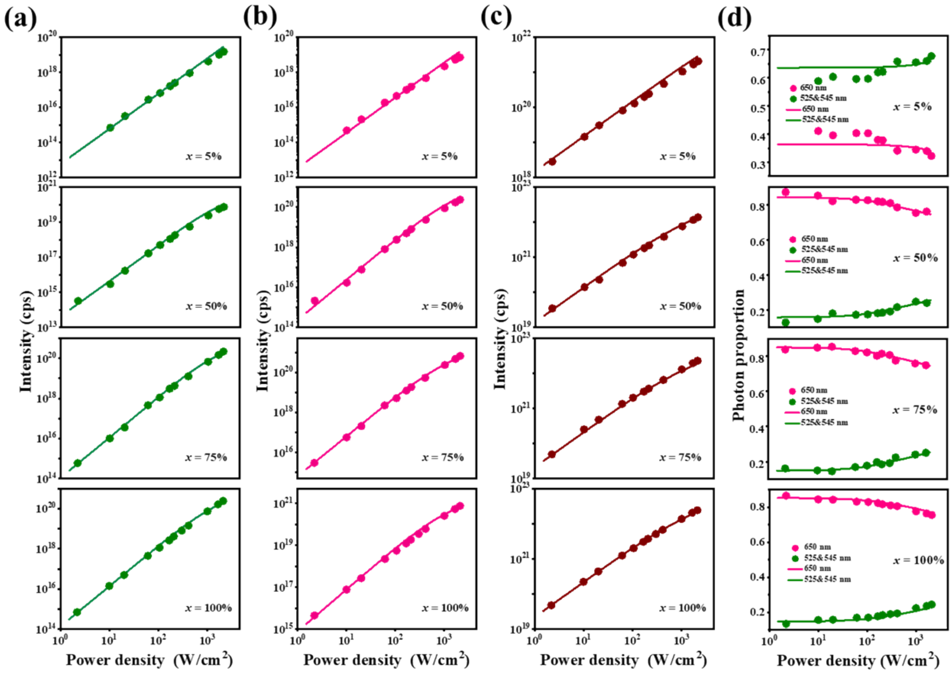

Figure S11. Experimental (colored dots) and simulated (solid lines) intensities for the $NaEr_xY_{1-x}F_4@NaYF_4$ (x=5, 50, 75, 100 %) nanoparticles. (a) Green emission at 525&545 nm. (b) Red emission at 650 nm. (c) NIR emission at 1530 nm. (d) Photon proportion of UC emissions.

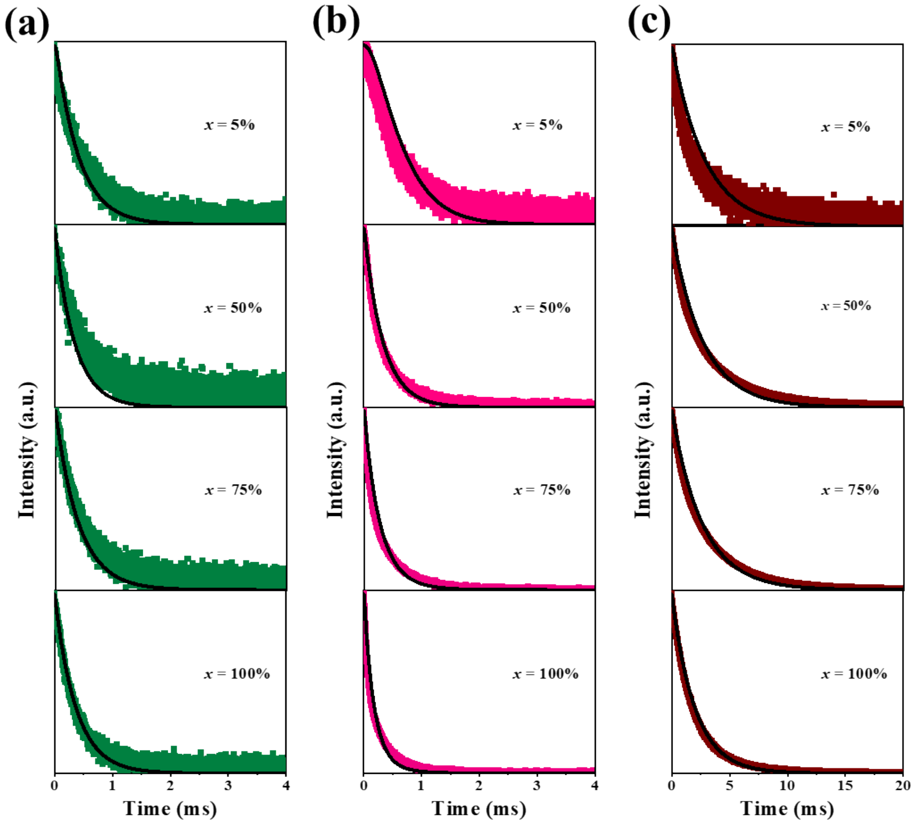

Figure S12. Experimental (colored dots) and simulated (solid lines) decay curves for the $NaEr_xY_{1-x}F_4@NaYF_4$ (x=5, 50, 75, 100 %) nanoparticles. (a) Green emission at 525&545 nm. (b) Red emission at 650 nm. (c) NIR emission at 1530 nm.

As shown in **Tables S1** and **S2**, we calculated the reduced chi-squared and R-square values for the time-domain spectrum under different Er concentrations. Most of the reduced chi-squared values are below 0.001, while the R-square values exceed 0.95, indicating minimal deviation between the simulated and actual values. However, due to the weak green emission and low signal-to-noise ratio, the calculated values for green emission are relatively worse than others.

Table S1. Chi-Squared values of the fitting time-domain spectrum

	100%	75%	50%	5%
NIR	0.000117	0.000246	0.000492	0.00495
Red	0.00019	0.000289	0.000258	0.00468
Green	0.00154	0.00328	0.005146	0.00185

Table S2. R-Squared values of the fitting time-domain spectrum

	100%	75%	50%	5%
NIR	0.994428	0.990359	0.979838	0.832342
Red	0.971293	0.967067	0.978316	0.745395
Green	0.880431	0.802919	0.709827	0.884296,

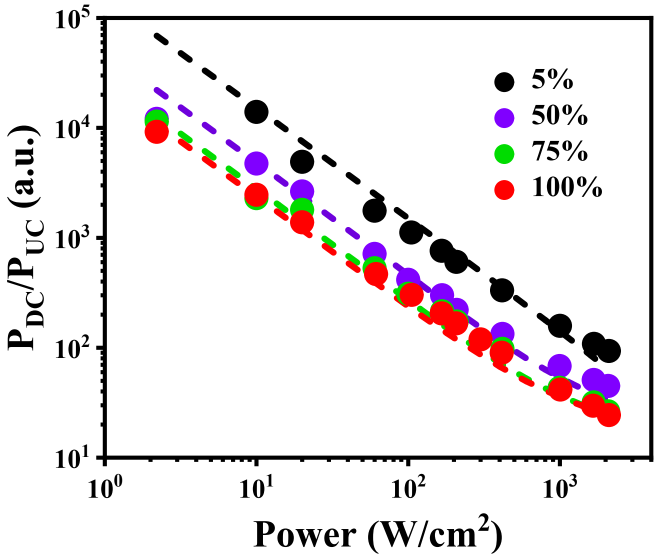

Figure S13. Power-dependent ratio of emitted photons between DC and UC processes in experiments (colored dot) and simulation (solid lines) for the NaEr$_x$Y$_{1-x}$F$_4$@NaYF$_4$ (x=5, 50, 75, 100 %) nanoparticles.

VI. Power-dependent simulated characteristics of decay curves.

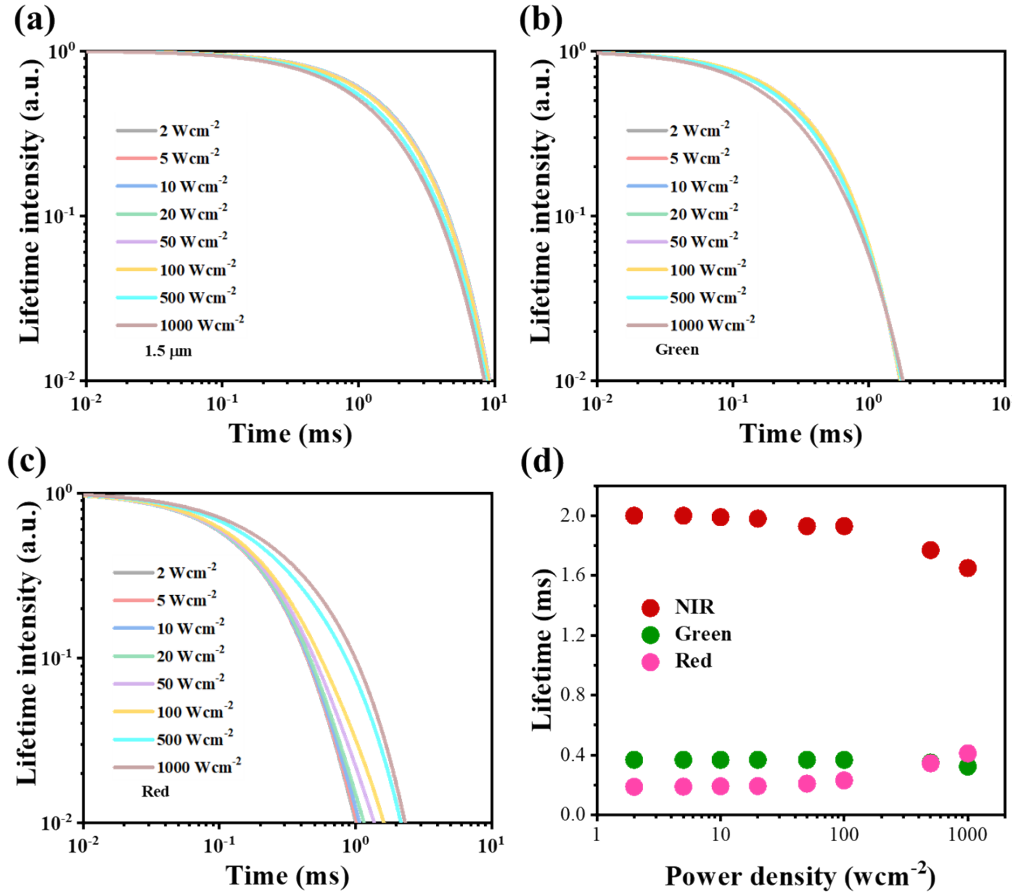

Figure S14. Power-dependent simulated decay curve and lifetime for different emissions. (a) NIR emission. (b) Green emission. (c) Red emission. (d) lifetime.

"In **Fig.S14**, we simulate the power-dependent decay curve for 100 NPs over a range of 2 Wcm^{-2} to 1000 Wcm^{-2}. When the power density is below 100 Wcm^{-2}, the lifetime at different wavelengths almost exhibits a power-independent characteristic. As the power density increases, the lifetimes of NIR and green emissions shorten due to population depletion caused by energy transfer upconversion. In contrast, the red emission lifetime is prolonged due to population enhancement from back energy transfer or cross-relaxation processes. Therefore, to determine the parameters of the rate equation model, the power density should be consistent with the experimental conditions."

VII. Emission enhancement of core-shell structure.

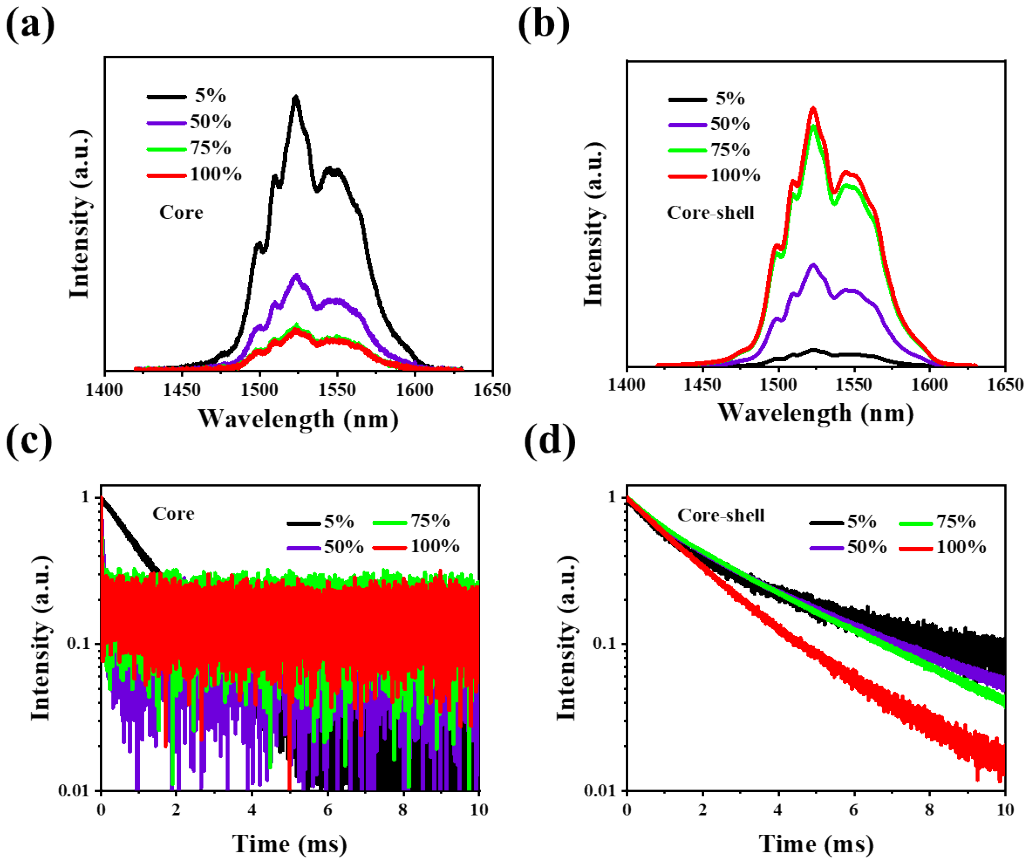

Figure S15. (a) DC emission of the core nanoparticles. (b) DC emission of the core-shell nanoparticles. (c) Decay curves at 1.5 μm of the core nanoparticles. (d) Decay curves at 1.5 μm of the core-shell nanoparticles with different Er concentrations (x=5, 50, 75, 100 %).

In pure core $NaEr_xY_{1-x}F_4$ nanoparticles, the intensity decreases rapidly with increasing Er concentration, as shown in **Fig.S15a**. The $NaEr_xY_{1-x}F_4@NaYF_4$ nanoparticles with the core-shell structure effectively alleviate surface quenching in the DC emission (**Fig.S15b**). In our time-resolved measurements, the decay processes decrease rapidly when the Er concentration in the core nanoparticles reaches 50% (**Fig.S15c**). The concentration quenching in these compositions is mainly caused by the surface effects reported in the past[5]. Therefore, the $NaYF_4$ shell protects the core from environmental influences. Compared with the pure core structure, the core-shell structure with high Er concentrations significantly improves the lifetimes (**Fig.S15d**).

VIII. Rate equation simulation of ENPCs.

The previous simulation results of the $NaEr_{0.02}Yb_{0.2}Y_{0.78}F_4$ nanoparticles (ENPCs) provide an important reference to determine energy transfer (ET) parameters. We then modified the ET parameters based on our experimental results by considering both UC and DC emissions. **Fig.S16** shows the energy level diagram, including relevant parameters. Among these parameters, σ_{ij}, k_{ij}, A_{ij} and W_{ij} represent the rates of GSA, ET, SE, and NR process from energy level *i* to *j*, respectively. N_{Er}, N_{Yb}, and ρ represent Er density, Yb density, and excitation photon density respectively. A_{Yb} and W_{Yb} represent the SE, and NR processes of N_{Yb1} energy level.

The population N_i of certain Er energy levels in ENPCs is described as

$$\frac{dN_0}{dt} = W_{10}N_1 + \sum_{i=1}^{7} A_{i0}N_i + k_{13}N_1^2 + k_{20}N_2N_{Yb0} - \left(k_{31}N_3 + k_{02}N_{Yb1}\right)N_0$$

$$\frac{dN_1}{dt} = W_{21}N_2 + \sum_{i=2}^{7} A_{i1}N_i + 2k_{31}N_3N_0 - \left(W_{10} + A_{10} + k_{14}N_{Yb1}\right)N_1 - 2k_{13}N_1^2$$

$$\frac{dN_2}{dt} = W_{32}N_3 + \sum_{i=4}^{7} A_{i2}N_i + k_{02}N_0N_{Yb1} + k_{62}N_6N_{Yb0} - \left(W_{21} + \sum_{j=0}^{1} A_{2j} + k_{20}N_{Yb0} + k_{26}N_{Yb1}\right)N_2$$

$$\frac{dN_3}{dt} = W_{43}N_4 + \sum_{i=5}^{7} A_{i3}N_i + k_{13}N_1^2 - \left(W_{32} + \sum_{j=0}^{1} A_{3j} + k_{31}N_0\right)N_3$$

$$\frac{dN_4}{dt} = W_{54}N_5 + A_{74}N_7 + k_{14}N_1N_{Yb1} + k_{84}N_8N_{Yb0} - \left(W_{43} + \sum_{j=0}^{2} A_{4j} + k_{47}N_{Yb1}\right)N_4$$

$$\frac{dN_5}{dt} = W_{65}N_6 - \left(W_{54} + \sum_{j=0}^{3} A_{5j} + k_{58}N_{Yb1}\right)N_5$$

$$\frac{dN_6}{dt} = W_{76}N_7 + k_{26}N_2N_{Yb1} - \left(W_{65} + \sum_{j=0}^{3} A_{6j} + k_{62}N_{Yb0}\right)N_6$$

$$\frac{dN_7}{dt} = W_{87}N_8 + k_{47}N_4N_{Yb1} - \left(W_{76} + \sum_{j=0}^{4} A_{7j}\right)N_7$$

$$\frac{dN_8}{dt} = k_{84}N_{Yb0}N_8 + k_{58}N_{Yb1}N_5 - W_{87}N_8$$

$$N_{Er} = N_0 + N_1 + N_2 + N_3 + N_4 + N_5 + N_6 + N_7 + N_8$$

The population of certain Yb energy levels is described as

$$\frac{dN_{Yb0}}{dt} = \left(A_{Yb} + W_{Yb} + k_{02}N_0 + k_{14}N_1 + k_{26}N_2 + k_{47}N_4 + k_{58}N_5\right)N_{Yb1}$$
$$-\left(\sigma_{02}\rho + k_{20}N_2 + k_{62}N_6 + k_{84}N_8\right)N_{Yb0}$$

$$\frac{dN_{Yb1}}{dt} = \left(\sigma_{02}\rho + k_{20}N_2 + k_{62}N_6 + k_{84}N_8\right)N_{Yb0}$$
$$-\left(A_{Yb} + W_{Yb} + k_{02}N_0 + k_{14}N_1 + k_{26}N_2 + k_{47}N_4 + k_{58}N_5\right)N_{Yb1}$$

$$N_{Yb} = N_{Yb1} + N_{Yb0}$$

We carefully construct the REs model in SI section VI. In the ENPCs, the ET transfer rate from Yb to Er depends on the higher Yb concentration^{6}. We adopted the original value of ENPCs from past work$^{6-8}$. Then, we adjust the parameters by fitting the power-dependent properties of the UC and DC emissions, including the emission intensities, and time-resolve processes at different wavelengths (**Fig.S16**). Tables S7-9 summarize the fitted values of ENPCs.

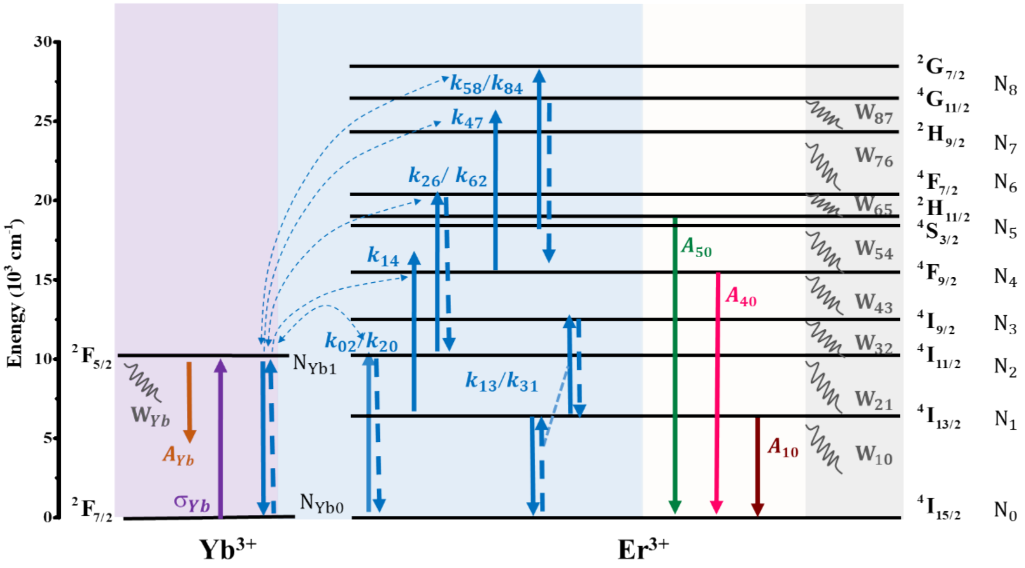

Figure S16. Energy level diagram of Er-Yb co-doping system illustrating the nominal parameters of the nine-level rate equation model in the ENPCs. The parameters of the SE process are shown in **Fig.S10**.

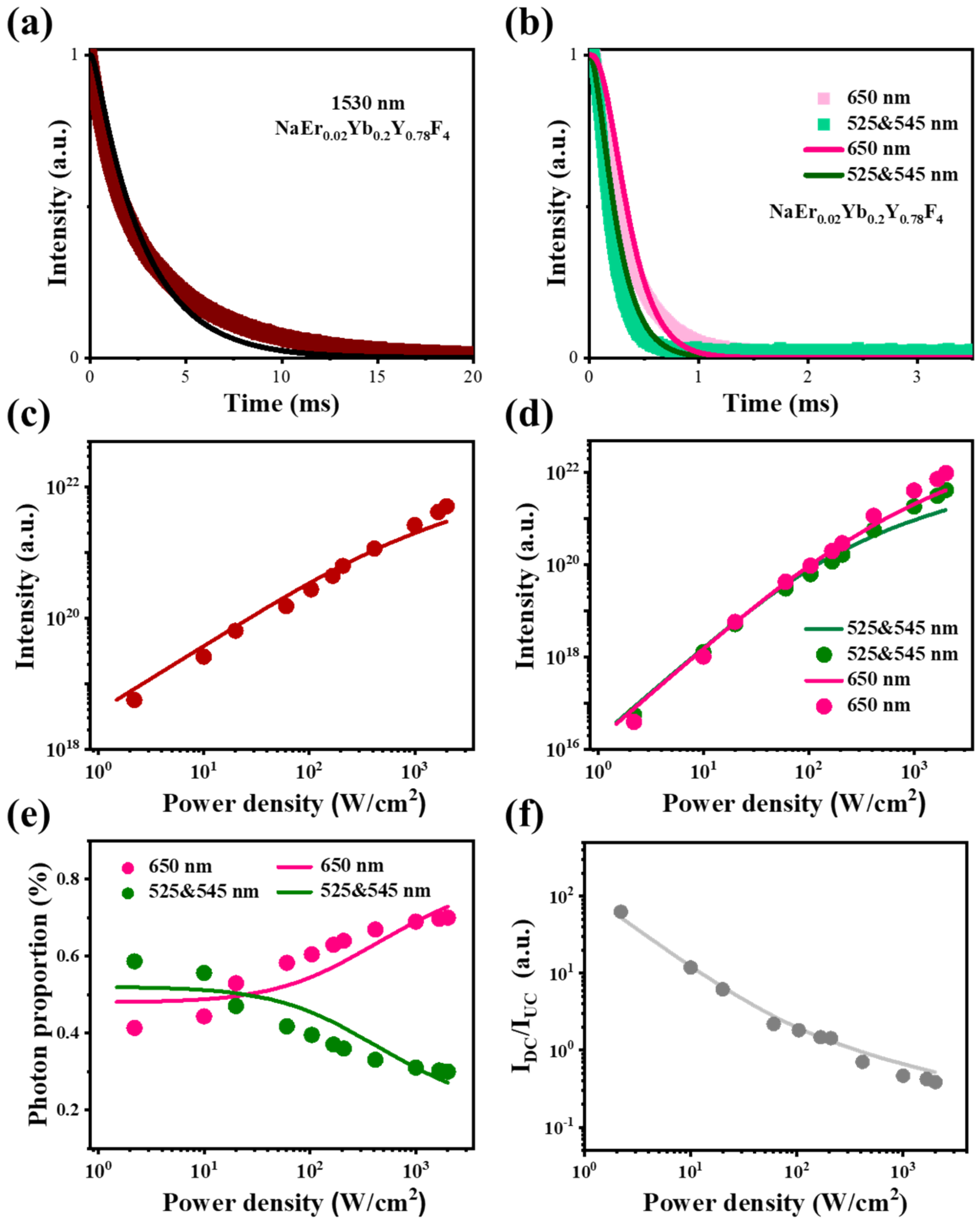

Figure S17. Experimental (colored dots) and simulated (solid lines) result for ENPCs. (a) Decay curves of NIR emission at 1530 nm. (b) Decay curves of green and red at 525&545 nm and 650 nm, respectively. (c) Intensity of NIR emission at 1530 nm. (d) Intensities of green and red at 525&545 nm and 650 nm, respectively. (e) Photon proportion of the green and red emission. (f) Power-dependent ratio of emitted photons between DC and UC processes.

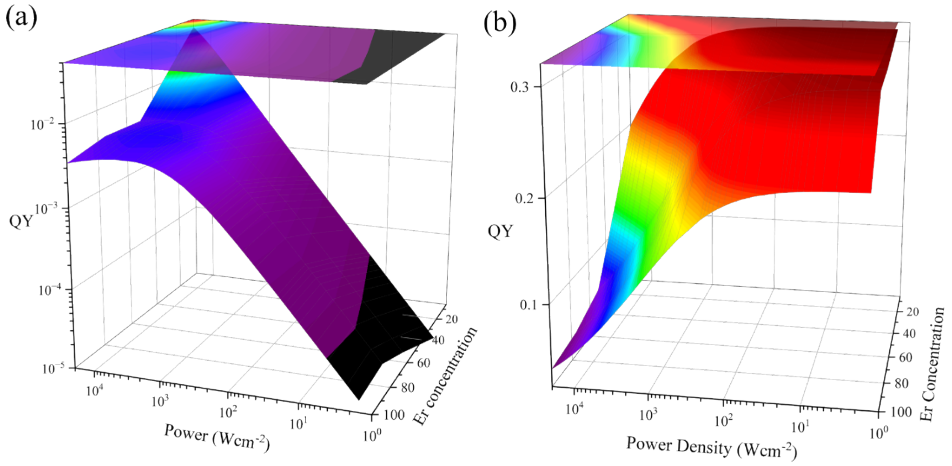

Figure S18. (a) Simulated power-dependent UCQY at different concentrations. (b) Simulated power-dependent DCQY at different concentrations.

As shown in **Fig. S18**, the UCQY at high erbium concentrations saturates beyond 10^3 Wcm^{-2}, remaining below 0.5%. While the DCQY can reach nearly 30% owing to the drastic $^4I_{11/2}$ - $^4I_{13/2}$ transition.

IX. Results of simulated parameters.

Table S3. The ion density and absorption cross-section

Parameter	Description	Value
N_{Er}	The density of Er^{3+} in the $NaEr_xY_{1-x}F_4$@$NaYF_4$ (x=5,50%,75%,100%)	$x\times1.35\times10^{22}$ cm^{-3}
N_{Er} (CNPs)	The density of Er^{3+} in the $NaEr_{0.02}Yb_{0.2}Y_{0.78}F_4$	2.7×10^{20} cm^{-3}
N_{Yb}	The density of Yb^{3+} in the $NaEr_{0.02}Yb_{0.2}Y_{0.78}F_4$	2.7×10^{21} cm^{-3}
σ_{Er}	The absorption cross-section of Er^{3+}	1.5×10^{-21} cm^{-2}
σ_{Yb}	The absorption cross-section of Yb^{3+}	8×10^{-21} cm^{-2}

Table S4. The radiative constants A_{ij} of Er (s^{-1})

	1	2	3	4	5	7
0	110	59	18	1835	1057	932
1		14	39	102	378	979
2				102	76	326
3					1	10
4						93

Table S5. The nonradiative constants of Er in $NaEr_xY_{1-x}F_4$@$NaYF_4$ (s^{-1})

$NaEr_xY_{1-x}F_4$@$NaYF_4$	5%	50%	75%	100%
W_{10}	240	260	265	390
W_{21}	13000	145000	225000	280000
W_{32}	7000	10000	12000	15000
W_{43}	1020	1500	1900	3950
W_{54}	930	1450	950	1200
W_{65}	1000000	1000000	1000000	1000000
W_{76}	200000	200000	200000	200000
W_{87}	1000000	1000000	1000000	1000000

Table S6. The Energy transfer rate in $NaEr_xY_{1-x}F_4$@$NaYF_4$ (cm^3s^{-1})

$NaEr_xY_{1-x}F_4$@$NaYF_4$	5%	50%	75%	100%
k_{14}	8.88×10^{-20}	9.25×10^{-18}	2×10^{-17}	3.4×10^{-17}
k_{26}	8.5×10^{-17}	6.83×10^{-15}	2.01×10^{-14}	4.2×10^{-14}
k_{62}	5×10^{-18}	7.65×10^{-16}	7.3×10^{-16}	1.06×10^{-15}
k_{47}	3.75×10^{-16}	1×10^{-14}	1.55×10^{-14}	2.1×10^{-14}
k_{58}	2×10^{-16}	$1.\ 2\times10^{-14}$	1.38×10^{-14}	1.5×10^{-14}
k_{84}	5×10^{-18}	5×10^{-16}	1.13×10^{-15}	2×10^{-15}
k_{13}	9.38×10^{-19}	2.5×10^{-16}	8.44×10^{-16}	1.5×10^{-15}
k_{31}	4.38×10^{-19}	1.69×10^{-16}	3.8×10^{-16}	6.75×10^{-16}
k_{54}	1.75×10^{-19}	1.75×10^{-17}	3.94×10^{-17}	7×10^{-17}

Table S7. The nonradiative constants of Er in ENPCs (s^{-1})[6-8]

$NaEr_{0.02}Yb_{0.2}Y_{0.78}F_4$	**Ours**	**[6]**	**[7]**	**[8]**
W_{10}	270	240	500	72.5
W_{21}	2600	1000	97800	18300
W_{32}	8500	100	22900	26400
W_{43}	6500	0	0	3260
W_{54}	4500	820	35	167
W_{65}	1000000	1000000	1000000	1310000
W_{76}	200000	50000	42500	50800
W_{87}	1000000	2500000	1060000	1460000

Table S8. The Energy transfer rate in ENPCs (cm^3s^{-1})

$NaEr_{0.02}Yb_{0.2}Y_{0.78}F_4$	**Ours**	**[6]**	**[7]**	**[8]**
k_{02}	7.5×10^{-16}	5.2×10^{-18}	1.1×10^{-16}	1.75×10^{-16}
k_{20}	2.5×10^{-16}	3.47×10^{-16}	2×10^{-16}	1.18×10^{-16}
k_{14}	8.1×10^{-19}	2.17×10^{-17}	0	0
k_{26}	3×10^{-15}	8.67×10^{-14}	2.5×10^{-15}	5.1×10^{-15}
k_{62}	5.8×10^{-16}	6.93×10^{-17}	2.15×10^{-16}	2.07×10^{-16}
k_{47}	3.9×10^{-16}	1.56×10^{-16}	0	2.86×10^{-15}
k_{58}	4.3×10^{-15}	1.73×10^{-14}	7.9×10^{-16}	1.36×10^{-15}
k_{84}	1.35×10^{-16}	1.56×10^{-16}	3.44×10^{-16}	4.12×10^{-16}
k_{13}	1.2×10^{-18}	2.31×10^{-17}	6.54×10^{-18}	$1.\ 7\times10^{-17}$
k_{31}	6×10^{-19}	8.04×10^{-19}	8.89×10^{-19}	1.37×10^{-18}

Table S9. The radiative and nonradiative constants of Yb (s^{-1})

A_{Yb}	The radiative constant in the $NaEr_{0.02}Yb_{0.2}Y_{0.78}F_4$	525
W_{Yb}	The nonradiative constant in the $NaEr_{0.02}Yb_{0.2}Y_{0.78}F_4$	5000

Table S10. The values of B_{ij}, C_{ij}, and D_{ij} in curve-fitting for all the parameters

k_{ij}	k_{14}	k_{26}	k_{62}	k_{47}	k_{58}	k_{84}	k_{13}	k_{31}	k_{54}
B_{ij}	3.45×10^{-21}	3.99×10^{-18}	1.21×10^{-19}	2.34×10^{-18}	1.87×10^{-18}	2×10^{-19}	1.48×10^{-19}	6.75×10^{-20}	7×10^{-21}
W_{ij}	W_{10}	W_{21}	W_{32}	W_{43}	W_{54}				
C_{ij}	0.0145	30.35	0.775	0.288	0.027				
D_{ij}	223	12000	7485	786	882				

X. Analytical calculation of simplified rate equations.

The relationship can be derived from the simplified four-level REs model when the UC emission is weak. The model consists of the N_0, N_1, N_2, and N_{UC} (we simplify the energy levels N_6, N_5, and N_4 as one state N_{UC} and neglect other energy levels for convenient calculation) as shown in the following equations.

$$\frac{dN_{\mathrm{UC}}}{dt} = k_{26}N_2^2 - \left(W_{NR} + A_{SE}\right)N_{UC} \qquad ①$$

$$\frac{dN_2}{dt} = \sigma_{02}\rho N_0 + W_{NR}N_{UC} - k_{26}N_2^2 - \left(W_{21} + A_{20}\right)N_2 \qquad ②$$

$$\frac{dN_1}{dt} = W_{21}N_2 - \left(W_{10} + A_{10}\right)N_1 \qquad ③$$

$$N_{Er} = N_0 + N_1 + N_2 + N_{UC} \qquad ④$$

Where W_{NR} and A_{SE} are the NR rate and SE rate at the N_{UC} state. When the UC emission is weak, we can neglect the small $k_{26}N_2^2$ and $W_{NR}N_6$ values in equation ②. Solving the steady-state REs, we obtain the analytical expression of the UC process:

$$N_{UC} = \frac{k_{26}}{\left(W_{NR} + A_{SE}\right)}\left(\frac{\sigma_{02}\rho N_{\mathrm{Er}}}{\left(W_{21} + A_{20}\right)}\right)^2 \propto \frac{k_{26}}{{W_{21}}^2} \qquad ⑤$$

The UC intensity is inversely proportional to the quadratic of W_{21}. We extract the expression of the power-dependent ratio between the UC and DC emissions from the simplified four-level REs model ①②③④, as.

$$\frac{P_{DC}}{P_{UC}} = \frac{A_{10}N_1}{A_{SE}N_{\mathrm{UC}}} = \frac{A_{10}W_{21}\left(W_{NR} + A_{SE}\right)\left(W_{21} + A_{20}\right)}{A_{SE}\sigma_{02}N_{\mathrm{Er}}k_{26}\rho\left(W_{10} + A_{10}\right)} \propto \frac{{W_{21}}^2}{\rho} \qquad ⑥$$

This ratio is inversely proportional to the power density as we measured. Due to the large W_{21}, the DC emission dominates the spectral distributions in 100_NPs. Extracted from the simplified four-level REs model ①②③④, the UCQY is given by:

$$\mathrm{UCQ}Y = \frac{A_{SE}k_{26}\sigma_{02}\rho N_{\mathrm{Er}}}{\left(W_{NR} + A_{SE}\right)\left(W_{21} + A_{20}\right)^2} \propto \frac{\rho}{{W_{21}}^2} \qquad ⑦$$

From the above equation, we notice that UCQY is linearly dependent on the power density as the measured value at low excitation power density.

References

1. Hudry, D.; Howard, I. A.; Popescu, R.; Gerthsen, D.; Richards, B. S., Structure-Property Relationships in Lanthanide-Doped Upconverting Nanocrystals: Recent Advances in Understanding Core-Shell Structures. *Adv Mater* **2019,** *31* (26), e1900623.

2. Boyer, J. C.; van Veggel, F. C., Absolute quantum yield measurements of colloidal NaYF4: Er3+, Yb3+ upconverting nanoparticles. *Nanoscale* **2010,** *2* (8), 1417-9.

3. Nicholls, A., Confidence limits, error bars and method comparison in molecular modeling. Part 1: the calculation of confidence intervals. *Journal of Computer-Aided Molecular Design* **2014,** *28* (9), 887-918.

4. Yan, L.; Zhou, B.; Song, N.; Liu, X.; Huang, J.; Wang, T.; Tao, L.; Zhang, Q., Self-sensitization induced upconversion of Er^{3+} in core－shell nanoparticles. *Nanoscale* **2018,** *10* (37), 17949-17957.

5. Johnson, N. J. J.; He, S.; Diao, S.; Chan, E. M.; Dai, H.; Almutairi, A., Direct Evidence for Coupled Surface and Concentration Quenching Dynamics in Lanthanide-Doped Nanocrystals. *Journal of the American Chemical Society* **2017,** *139* (8), 3275-3282.

6. Kaiser, M.; Würth, C.; Kraft, M.; Soukka, T.; Resch-Genger, U., Explaining the influence of dopant concentration and excitation power density on the luminescence and brightness of β-$NaYF_4$:Yb^{3+},Er^{3+} nanoparticles: Measurements and simulations. *Nano Research* **2019,** *12* (8), 1871-1879.

7. Hossan, M. Y.; Hor, A.; Luu, Q.; Smith, S. J.; May, P. S.; Berry, M. T., Explaining the Nanoscale Effect in the Upconversion Dynamics of β-$NaYF_4$:Yb^{3+}, Er^{3+} Core and Core－Shell Nanocrystals. *The Journal of Physical Chemistry C* **2017,** *121* (30), 16592-16606.

8. Pini, F.; Frances-Soriano, L.; Peruffo, N.; Barbon, A.; Hildebrandt, N.; Natile, M. M., Spatial and Temporal Resolution of Luminescence Quenching in Small Upconversion Nanocrystals. *ACS Applied Materials & Interfaces* **2022,** *14* (9), 11883-11894.